

$N_f = 2 + 1$ dynamical Wilson quark simulation toward the physical point

Yoshinobu Kuramashi* for the PACS-CS Collaboration

*Center for Computational Sciences and Graduate School of Pure and Applied Sciences,
University of Tsukuba, Tsukuba, Ibaraki 305-8571, Japan*

We present preliminary results of the PACS-CS project which simulates 2+1 flavor lattice QCD toward the physical point with the nonperturbatively $O(a)$ -improved Wilson quark action and the Iwasaki gauge action. Calculations are carried out at $\beta = 1.9$ on a $32^3 \times 64$ lattice with the use of the domain-decomposed HMC algorithm to reduce the up-down quark mass. The resulting pseudoscalar meson masses range from 730 MeV down to 210 MeV. We discuss the physical results including the chiral analysis in the pseudoscalar meson sector and the hadron spectrum. Some algorithmic issues are also discussed.

*The XXV International Symposium on Lattice Field Theory
July 30-4 August 2007
Regensburg, Germany*

*E-mail: kuramasi@het.ph.tsukuba.ac.jp

1. Introduction

The first lattice QCD calculation of hadron masses in 1981 revealed its potential ability to non-perturbatively evaluate the physical quantities in the strong interaction from first principles. Since then, the history of lattice QCD has been a succession of enduring efforts to control the major systematic errors due to finite lattice size, finite lattice spacing, quenching and chiral extrapolation. Thanks to recent progress of simulation algorithms and increasing availability of computational resources, we are about to bring all the above systematic errors under control. This will allow us to establish whether or not QCD is the fundamental theory of the strong interaction by investigating the hadron spectrum, and further proceed to elucidate the fundamental issues of the strong interactions and the Standard Model.

The previous CP-PACS/JLQCD project[1, 2] aimed at a full removal of the quenching effects by performing $N_f = 2 + 1$ lattice QCD simulations with the nonperturbatively $O(a)$ -improved Wilson quark action[3] and the Iwasaki gauge action[4] on a $(2 \text{ fm})^3$ lattice at three lattice spacings. While we have succeeded in incorporating the dynamical strange quark effects by the Polynomial Hybrid Monte Carlo (PHMC) algorithm[5], the lightest up-down quark mass reached with the HMC algorithm was 64 MeV corresponding to $m_\pi/m_\rho \approx 0.6$, which required a long chiral extrapolation to the physical point at $m_\pi/m_\rho \approx 0.18$.

The PACS-CS(Parallel Array Computer System for Computational Science) project[6, 7, 8] is the successor to the CP-PACS/JLQCD project, which takes up the task that the latter has left off, namely simulation at the physical point to remove the ambiguity of chiral extrapolation. It employs the same quark and gauge actions as the CP-PACS/JLQCD project, but uses the PACS-CS computer with a total peak speed of 14.3 TFLOPS developed and installed at University of Tsukuba on 1 July 2006. The up-down quark masses are reduced by employing the domain-decomposed HMC (DDHMC) algorithm with the replay trick proposed by Lüscher[9, 10]. So far, we have reached the up-down quark mass of 6 MeV which yields the pion mass of about 210 MeV. We also improve the simulation of the strange quark part with the UV-filtered PHMC (UV-PHMC) algorithm[11].

In this report we present simulation details and preliminary results which include the chiral analysis on the pseudoscalar meson masses and the decay constants with chiral perturbation theory, the light hadron spectrum and the ρ - $\pi\pi$ mixing effects. Some algorithmic issues are also discussed. Selected topics on the light hadron spectrum and the ChPT analysis on the pseudoscalar meson masses and the decay constants are also reported in Refs.[12, 13].

2. Simulation details

2.1 Simulation parameters

We employ the $O(a)$ -improved Wilson quark action with a nonperturbative improvement coefficient $c_{\text{SW}} = 1.715$ [3] and the Iwasaki gauge action at $\beta = 1.90$ on a $32^3 \times 64$ lattice which is enlarged from $20^3 \times 40$ in the CP-PACS/JLQCD project to investigate the baryon masses. Simulation parameters are summarized in Table 1. We choose six combinations of the hopping parameters $(\kappa_{\text{ud}}, \kappa_{\text{s}})$ based on the previous CP-PACS/JLQCD results. Among them the heaviest combination $(\kappa_{\text{ud}}, \kappa_{\text{s}}) = (0.13700, 0.13640)$ in this work is the lightest one in the previous CP-PACS/JLQCD simulations, which enable us to make a direct comparison of the two results with different lattice

sizes. As for the strange quark, the hopping parameter $\kappa_s = 0.13640$ corresponds to the physical point $\kappa_s = 0.136412(50)$ as estimated in the CP-PACS/JLQCD work[1, 2]. This is the reason why all our simulations are carried out with $\kappa_s = 0.13640$, the one exception being the run at $\kappa_s = 0.13660$ and $\kappa_{ud} = 0.13754$ to investigate the strange quark mass dependence.

In order to simulate the degenerate up-down quarks we employ the DDHMC algorithm, whose effectiveness for small quark mass region has already been shown in the $N_f = 2$ case[9, 14, 15]. The characteristic feature of this algorithm is a geometric separation of the up-down quark determinant into the UV and the IR parts as a preconditioner of HMC, which is implemented by domain-decomposing the full lattices with small blocks. We choose 8^4 for the block size being less than $(1 \text{ fm})^4$ in physical units and small enough to reside within a computing node of the PACS-CS computer. There are two prominent points in the DDHMC algorithm. Firstly, communication between the computing nodes is not required in calculating the UV part, which is a preferable feature for alleviating the problem of a widening gap between the processor floating point performance and the network communication bandwidth with parallel computers. Secondly, we can incorporate the multiple time scale integration scheme[16] to reduce the simulation cost efficiently. The relative magnitudes of the force terms are found to be

$$\|F_g\| : \|F_{UV}\| : \|F_{IR}\| \approx 16 : 4 : 1, \quad (2.1)$$

where we adopt the convention $\|M\|^2 = -2\text{tr}(M^2)$ for the norm of an element M of the SU(3) Lie algebra. F_g denotes the gauge part and $F_{UV,IR}$ are for the UV and the IR parts of the up-down quarks. The associated step sizes for the forces are controlled by three integers $N_{0,1,2}$: $\delta\tau_g = \tau/N_0N_1N_2$, $\delta\tau_{UV} = \tau/N_1N_2$, $\delta\tau_{IR} = \tau/N_2$ with τ the trajectory length. The integers $N_{0,1,2}$ are chosen such that

$$\delta\tau_g\|F_g\| \approx \delta\tau_{UV}\|F_{UV}\| \approx \delta\tau_{IR}\|F_{IR}\|. \quad (2.2)$$

Taking account of the relative magnitudes of the forces in eq.(2.1) we find a larger value is allowed for $\delta\tau_{IR}$ compared to $\delta\tau_g$ and $\delta\tau_{UV}$, which means that we need to calculate F_{IR} less frequently in the molecular dynamics trajectories. Since the calculation of F_{IR} contains the quark matrix inversion on the full lattice, which is the most time consuming part, this integration scheme saves the simulation cost remarkably. The values for $N_{0,1,2}$ are listed in Table 1, where N_0 and N_1 are fixed

κ_{ud}	κ_s	τ	(N_0, N_1, N_2)	N_{poly}	MD time	$\tau_{int}[P]$
0.13700	0.13640	0.5	(4,4,10)	180	2000	38.2(17.3)
0.13727	0.13640	0.5	(4,4,14)	180	2000	20.9(10.2)
0.13754	0.13640	0.5	(4,4,20)	180	2500	19.2(8.6)
	0.13660	0.5	(4,4,28)	220	900	10.3(2.9)
0.13770	0.13640	0.25	(4,4,16)	180	2000	38.4(25.2)
0.13781	0.13640	0.25	(4,4,48)	180	350	9.1(6.1)

Table 1: Simulation parameters. MD time is the number of trajectories multiplied by the trajectory length τ . $\tau_{int}[P]$ denotes the integrated autocorrelation time for the plaquette.

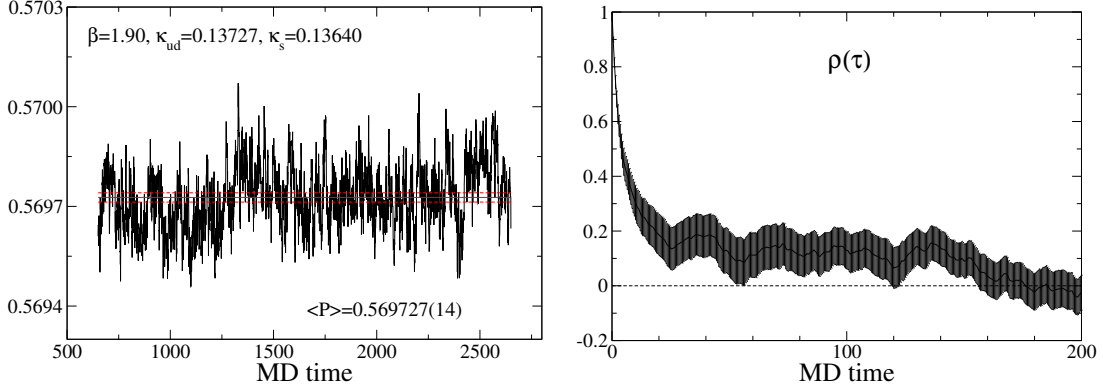


Figure 1: Plaquette history (left) and normalized autocorrelation function (right) for $(\kappa_{ud}, \kappa_s) = (0.13727, 0.13640)$. Horizontal lines in the left denote the average value of the plaquette with an error band.

at 4 for all the hopping parameters, while the value of N_2 is adjusted taking account of acceptance rate and simulation stability.

For the UV-PHMC algorithm for the strange quark, the domain-decomposition is not implemented. Since we have found $\|F_s\| \approx \|F_{IR}\|$, the step size is chosen as $\delta\tau_s = \delta\tau_{IR}$. The polynomial order for UV-PHMC, which is denoted by N_{poly} in Table 1, is adjusted to yield high acceptance rate for the global Metropolis test at the end of each trajectory.

The inversion of the Wilson-Dirac operator D on the full lattice is carried out by the SAP (Schwarz alternating procedure) preconditioned GCR solver, where the preconditioning can be accelerated with the single-precision arithmetic whereas the GCR solver is implemented with the double precision[17]. We employ the stopping condition $|Dx - b|/|b| < 10^{-9}$ for the force calculation and 10^{-14} for the Hamiltonian, which guarantees the reversibility of the molecular dynamics trajectories to high precision: $|\Delta U| < 10^{-12}$ for the link variables and $|\Delta H| < 10^{-8}$ for the Hamiltonian at $(\kappa_{ud}, \kappa_s) = (0.13781, 0.13640)$.

2.2 Plaquette history and autocorrelation time

In Fig. 1 we show the plaquette history and the normalized autocorrelation function $\rho(\tau)$ at $(\kappa_{ud}, \kappa_s) = (0.13727, 0.13640)$ as a representative case. The integrated autocorrelation time is estimated as $\tau_{int}[P] = 20.9(10.2)$ following the definition in Ref. [9]

$$\tau_{int}(\tau) = \frac{1}{2} + \sum_{0 < \tau \leq W} \rho(\tau), \quad (2.3)$$

where the summation window W is set to the first time lag τ that $\rho(\tau)$ becomes consistent with zero within the error bar. In this case we find $W = 119.5$. The choice of W is not critical for estimate of τ_{int} in spite of the long tail observed in Fig. 1. Extending the summation window, we find that $\tau_{int}[P]$ saturates at $\tau_{int}[P] \approx 25$ beyond $\tau = 200$, which is within the error bar of the original estimate. For other hopping parameters we have found similar behaviors for the plaquette history and the normalized autocorrelation function. We hardly observe the quark mass dependence for $\tau_{int}[P]$ listed in Table 1. The statistics may not be sufficiently large to derive a definite conclusion, however.

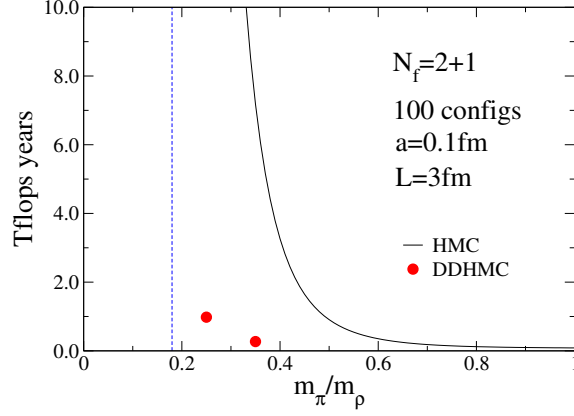


Figure 2: Cost estimate of $N_f = 2 + 1$ QCD simulations with the HMC (solid line) and the DDHMC (red circle) algorithms at $a = 0.1$ fm with $L = 3$ fm for 100 independent configurations. Vertical dotted line denotes the physical point.

3. Algorithmic issues

3.1 Efficiency of DDHMC algorithm

In order to discuss the efficiency of the DDHMC algorithm, it is instructive to compare with that of the HMC algorithm. We first recall an empirical cost formula for $N_f = 2$ QCD simulations with the HMC algorithm based on the CP-PACS results[18]:

$$\text{cost}[\text{Tflops} \cdot \text{years}] = C \left[\frac{\#\text{conf}}{1000} \right] \cdot \left[\frac{0.6}{m_\pi/m_\rho} \right]^6 \cdot \left[\frac{L}{3 \text{ fm}} \right]^5 \cdot \left[\frac{0.1 \text{ fm}}{a} \right]^7$$

with $C \approx 2.8$. A strong quark mass dependence is found in the above formula: $1/(m_\pi/m_\rho)^6$ behaves as $1/m_{\text{ud}}^3$ in the leading term for the small quark mass region. This quark mass dependence is owing to the following three factors: The number of the quark matrix inversion is governed by the condition number which should be proportional to $1/m_{\text{ud}}$; to keep the acceptance rate fixed we should take $\delta\tau \propto m_{\text{ud}}$ for the step size in the molecular dynamics trajectories; The autocorrelation time of the HMC evolution shows $1/m_{\text{ud}}$ dependences in the CP-PACS run[19].

To estimate the computational cost for $N_f = 2 + 1$ QCD simulations with the HMC algorithm, we assume that the strange quark contribution is given by half of eq.(3.1) at $m_\pi/m_\rho = 0.67$ which is a phenomenologically estimated ratio of the strange pseudoscalar meson “ m_{η_s} ” and m_ϕ :

$$\frac{m_{\eta_s}}{m_\phi} = \frac{\sqrt{2m_K^2 - m_\pi^2}}{m_\phi} \approx 0.67. \quad (3.1)$$

Since the strange quark is relatively heavy, its computational cost occupies only a small fraction as the up-down quark masses decrease. In Fig. 2 we draw the cost formula for the $N_f = 2 + 1$ case as a function of m_π/m_ρ , where we take $\#\text{conf}=100$, $a=0.1$ fm and $L = 3$ fm in eq.(3.1) as a representative case. We observe a steep increase of the computational cost below $m_\pi/m_\rho \simeq 0.5$. At the physical point the expected cost is $O(100)$ Tflops-years.

τ	(N_0, N_1, N_2)	N_{poly}	trajs.	MD time	$\tau_{\text{int}}[P]$	$\tau_{\text{int}}[\text{\#mult}]$
0.5	(4,4,6)	130	6000	3000	23.7(9.2)	92(56)
0.5/3	(4,4,2)	130	18000	3000	18.6(5.9)	42(21)

Table 2: Parameters for τ -dependence study. #mult denotes the number of multiplications of the Wilson-Dirac quark matrix on the full lattice.

Now let us turn to the case of the DDHMC algorithm. The red symbol denotes the measured cost at $\kappa_{\text{ud}}=0.13781, 0.13770$ with $\kappa_s = 0.13640$, which are the lightest two points in our simulation. The DDHMC algorithm show a remarkable improvement reducing the cost by 30 – 50 times in magnitude. The majority of this reduction arises from the multiple time scale integration scheme and the GCR solver accelerated by the SAP preconditioning with the single-precision arithmetic. Roughly speaking, the improvement factor is $O(10)$ for the former and 3 – 4 for the latter. Note that the quark mass dependence is also tamed: Since we find that $\tau_{\text{int}}[P]$ is independent of the quark masses, the cost is proportional to $1/m_{\text{ud}}^2$. Our results show a feasibility of simulations at the physical point with the $O(10)$ Tflops computer which is available at present.

3.2 τ dependence of DDHMC algorithm

In the DDHMC algorithm a subset of of all link variables, which are referred to as the active link variables, are updated during the molecular dynamics evolution, while keeping other field variables fixed[9]. The fraction of the active link variables depends on the block size we choose. In our case of 8^4 it is only 37%. To ensure that all the link variables on the lattice should be updated equally on average we implement random gauge field translations at the end of every molecular dynamics trajectories following Ref. [9].

Our concern is that the DDHMC algorithm might have a long autocorrelation time due to the existence of fixed link variables during the molecular dynamics evolution. A possible way to reduce the effects of the fixed link variables is more frequent random gauge field translations. This is easily realized by making τ shorter with $\delta\tau$ fixed. We investigate the τ dependence of the DDHMC algorithm employing a smaller lattice size of $16^3 \times 32$ at $(\kappa_{\text{ud}}, \kappa_s) = (0.13700, 0.13640)$. Other parameters are summarized in Table 2.

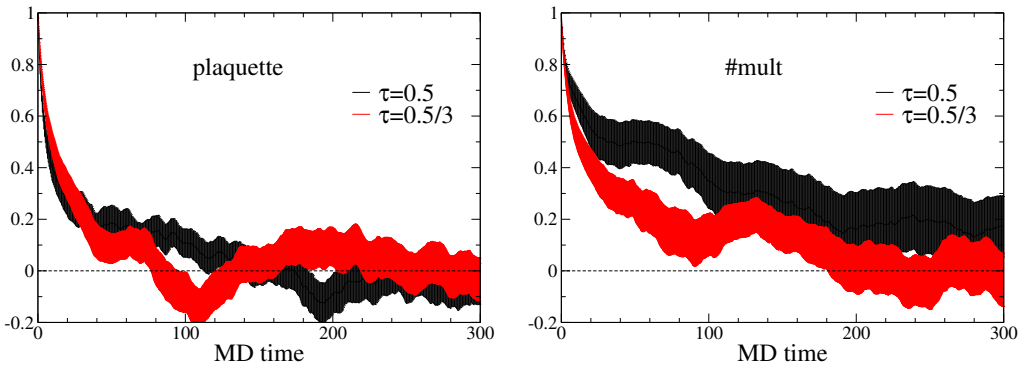


Figure 3: Normalized autocorrelation functions for the plaquette (left) and the #mult (right) at $(\kappa_{\text{ud}}, \kappa_s) = (0.13700, 0.13640)$. Black (red) symbols denote the $\tau = 0.5$ ($\tau = 0.5/3$) case.

In Fig. 3 we show the normalized autocorrelation functions for the plaquette and the number of multiplications of the Wilson-Dirac quark matrix on the full lattice during a molecular dynamics trajectory. Black symbols denote the $\tau = 0.5$ case, while red ones are for the $\tau = 0.5/3$ case. We observe that the normalized autocorrelation functions for $\tau = 0.5$ have longer tails than $\tau = 0.5/3$ before becoming consistent with zero: This is quantitatively checked by the integrated autocorrelation times $\tau_{\text{int}}[P]$ and $\tau_{\text{int}}[\#\text{mult}]$ in Table 2: The $\tau = 0.5/3$ case has shorter autocorrelation times. Since the computational cost is the same for the $\tau = 0.5$ and the $\tau = 0.5/3$ cases in terms of MD time, we can conclude that the $\tau = 0.5/3$ case shows a better efficiency than the $\tau = 0.5$ case. Based on this study, albeit conducted at a relatively heavy quark mass ($m_\pi/m_\rho \approx 0.6$), we employ $\tau = 0.25$ for the production run at $(\kappa_{\text{ud}}, \kappa_{\text{s}}) = (0.13781, 0.13640)$ and $(0.13770, 0.13640)$, which is half of the trajectory length at other hopping parameters.

3.3 Simulation stability

In Refs. [14, 15] simulation stability was discussed based on the spectral gap distribution of the Wilson-Dirac operator for two-flavor lattice QCD simulations. The spectral gap is defined as

$$\mu = \min\{|\lambda| \mid \lambda \text{ is an eigenvalue of } Q\}, \quad (3.2)$$

where Q is the hermitian Wilson-Dirac operator $Q = \gamma_5 D_W$ with $D_W = (1/2)\{\gamma_\mu(\nabla_\mu^* + \nabla_\mu) - a\nabla_\mu^* \nabla_\mu\} + m_0$. Important indices to characterize the distribution are its median $\bar{\mu}$ and width σ . The latter is defined as $(v - u)/2$, where $[u, v]$ is the smallest range of μ which contains more than 68.3% of the data. This is to avoid potentially large statistical uncertainties which might occur when data are not sufficiently sampled. Their chief findings are two points: The first one is that the median $\bar{\mu}$ shows a good linear dependence on the current up-down quark mass $m_{\text{ud}}^{\text{AWI}}$ and the magnitude of the slope is well described by Z_A empirically. The second one is that the width σ scales as

$$\sigma \frac{\sqrt{V}}{a} \simeq 1 \quad (3.3)$$

with V the four-dimensional volume in physical units. They also observe that the width σ is roughly independent of the quark mass for the unimproved Wilson quark action, while it shows a trend to decrease with the mass for the improved one.

This study was also applied to the $N_f = 2 + 1$ case in Ref. [8] where we reported on our preliminary run on a $16^3 \times 32$ lattice preparing for the PACS-CS project. We observed $\bar{\mu} \propto m_{\text{ud}}^{\text{AWI}}$ and found $0.5 \lesssim \sigma(\sqrt{V}/a) \lesssim 0.76$ for $15 \text{ MeV} < m_{\text{ud}}^{\text{AWI}} < 64 \text{ MeV}$, where σ diminishes as the up-down quark mass decreases.

The existence of a gap in the spectrum of the Wilson-Dirac operator allows us to simulate the light quarks efficiently. The authors in Ref. [14] propose a stability condition requiring $\bar{\mu} \geq 3\sigma$ to assure the existence of the gap. Let us apply this condition to our case. Assuming $\sigma(\sqrt{V}/a) = 1$ we estimate $\sigma = 2.26 \text{ MeV}$ using $a = 0.09 \text{ fm}$ and $V = (2.8 \text{ fm})^4$ which will be obtained later. By using the empirical relation $\bar{\mu} \simeq Z_A m_{\text{ud}}^{\text{AWI}}$ we find $Z_A m_{\text{ud}}^{\text{AWI}} \gtrsim 6.8 \text{ MeV}$ for the stability condition, which is heavier than the physical point. On the other hand, we found $\sigma(\sqrt{V}/a) < 1$ in Ref. [8], indicating that the actual bound will be lower. Our runs toward the physical point should shed light on the actual bound of stability for our lattice parameters.

prec.	block size	ρ	(N_0, N_1, N_2)	τ	MD time	P_{acc}
DD	8^4	—	(4,8,12)	1	3000	0.857(8)
mass	—	0.09	(4,8,12)	1	3000	0.794(8)

Table 3: Simulation parameters for the DDHMC and the mass-preconditioned HMC algorithms. P_{acc} denote the acceptance rate.

3.4 Comparison of DDHMC and mass-preconditioned HMC

As discussed in Sec. 3.1, it is essential for the efficiency of the DDHMC algorithm to incorporate the multiple time scale integration scheme. It is well known that this scheme is also applicable to the mass-preconditioned HMC algorithm[20, 21]. We have made a direct comparison of the two algorithms in $N_f = 2$ QCD on a $16^3 \times 32$ lattice employing the $O(a)$ -improved Wilson quark action with the nonperturbative improvement coefficient $c_{\text{SW}} = 2.0171$ [22] and the plaquette gauge action at $\beta = 5.2$. The lattice spacing is 0.1 fm and the physical pseudoscalar meson mass is about 600 MeV at $\kappa_{\text{ud}} = 0.1355$. For the mass-preconditioned HMC algorithm we employ two set of the pseudofermion fields which decompose the fermion determinant as

$$\det Q^2 = \det(W^\dagger W) \det\left(\frac{Q^2}{W^\dagger W}\right), \quad (3.4)$$

where Q is the hermitian Wilson-Dirac operator and the preconditioning operator is given by $W = Q + \rho$. For convenience we refer to $\det(W^\dagger W)$ as the UV part and the $\det(Q^2/(W^\dagger W))$ as the IR part in an analogy with the DDHMC algorithm. The step sizes are chosen with the three integers $N_{0,1,2}$ in exactly the same way as the DDHMC algorithm. Simulation parameters are summarized in Table 3. The block size for the DDHMC algorithm and the ρ parameter for the mass-preconditioned HMC algorithm are chosen such that $\|F_{0,1,2}\|$ are roughly the same between these two algorithms. This condition yields comparable acceptance ratios with $N_{0,1,2}$ in common. We employ the BiCGStab algorithm for the quark matrix inversion in both the UV and the IR parts.

In Fig. 4 we plot the normalized autocorrelation function for the plaquette as a function of MD time. The results of both algorithms show quite similar behaviors and the integrated autocorrelation

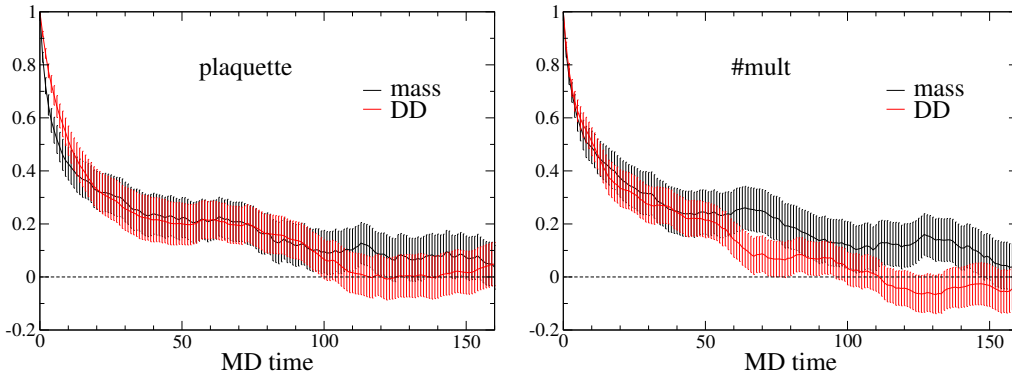


Figure 4: Normalized autocorrelation functions for the plaquette (left) and the number of multiplications of the Wilson-Dirac quark matrix on the full lattice (right). Black (red) symbols denote the DDHMC (mass-preconditioned HMC) case.

prec.	$\tau_{\text{int}}[P]$	$\tau_{\text{int}}[\#\text{mult}]$	$\#\text{mult}$	cost[P]	cost[$\#\text{mult}$]
DD	27(10)	22(7)	45530(280)	1.2(5)	1.0(3)
mass	28(12)	35(16)	67160(380)	1.9(8)	2.4(1.0)

Table 4: Integrated autocorrelation time and cost estimate for the DDHMC and the mass-preconditioned HMC algorithms.

time $\tau_{\text{int}}[P]$ in Table 4 are consistent within the errors. Figure 5 shows the MD-time history of the number of multiplications of the Wilson-Dirac quark matrix on the full lattice. The total number of multiplications is the sum of those required to calculate the UV and the IR forces and the Hamiltonian. Their contributions are denoted by black, red, green, blue lines in order. Comparing the results of the DDHMC and the mass-preconditioned HMC, we observe a clear difference in the UV part contribution: the mass-preconditioned HMC needs more than twice of the multiplication number for the DDHMC. This ends up in a 50% difference in the total number of multiplications. In Fig. 4 we also plot the normalized autocorrelation function for the total number of multiplications. Although the DDHMC result seems to show a slightly steeper fall-off, both results are consistent within the error bars. This is confirmed by the integrated autocorrelation time $\tau_{\text{int}}[\#\text{mult}]$ in Table 4.

Now let us compare the efficiencies of both algorithms. We define the machine-independent cost formula by

$$\text{cost}[\mathcal{O}] = \#\text{mult}(\text{total})/\text{MD time} \times \tau_{\text{int}}[\mathcal{O}]/10^6, \quad (3.5)$$

where the observable \mathcal{O} is the plaquette or the total number of multiplications. In Table 4 we summarize the results of $\text{cost}[\mathcal{O}]$. For both observables the DDHMC algorithm shows better efficiency than the mass-preconditioned HMC algorithm albeit the errors are rather large.

There remains a couple of concerns in this study. The first one is the quark mass dependence, because our results are obtained at only one hopping parameter. The second one is the optimization. While we choose 8^4 block size for the DDHMC algorithm and $\rho = 0.09$ for the mass-preconditioned HMC algorithm since $\|F_{0,1,2}\|$ are roughly the same, these parameters may not be the optimal values for each of the algorithms. We leave these issues to future studies.

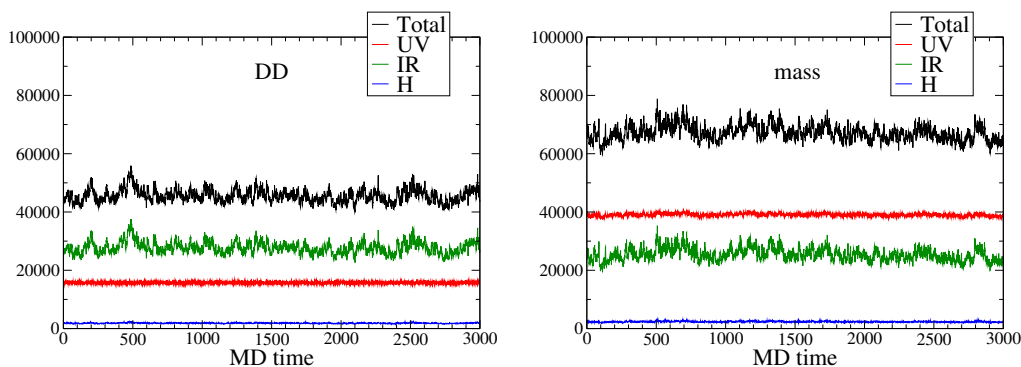


Figure 5: History for number of multiplications of the Wilson-Dirac quark matrix on the full lattice for the DDHMC algorithm (left) and the mass-preconditioned HMC algorithm (right).

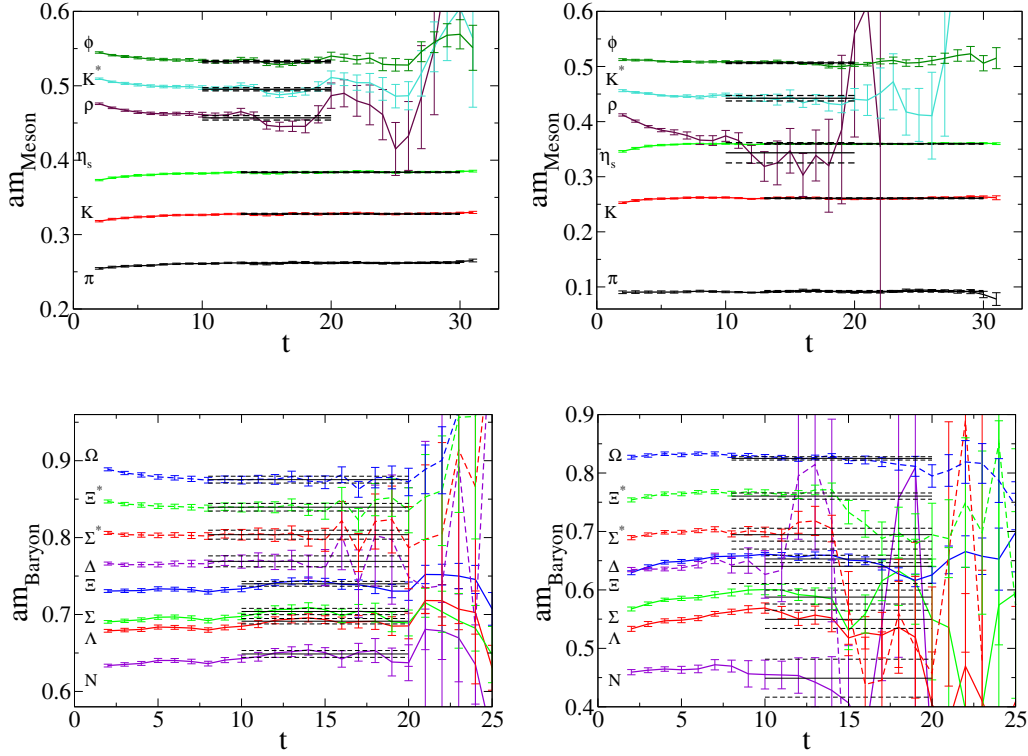


Figure 6: Effective masses for the mesons (top) and the baryons (bottom) at $\kappa_{ud} = 0.13727$ (left) and 0.13781 (right). Horizontal lines represent the fitting results with an error band.

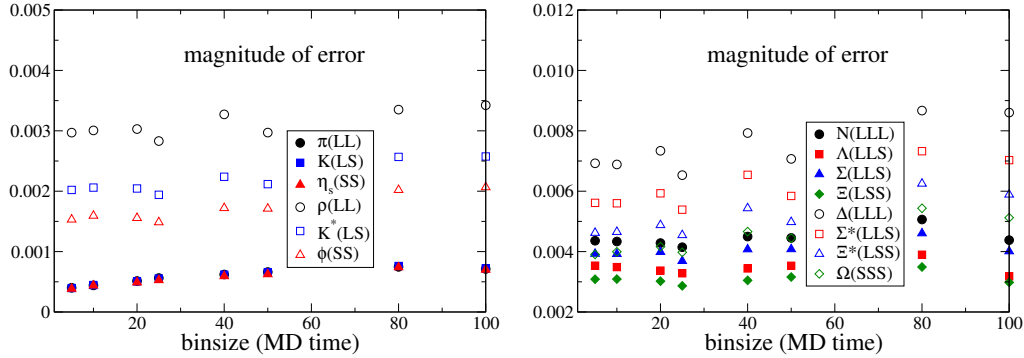


Figure 7: Binsize dependence of magnitude of error for mesons (left) and baryons (right) at $(\kappa_{ud}, \kappa_s) = (0.13727, 0.13640)$.

4. Physical results

4.1 Measurement of hadron masses, quark masses, decay constants

We measure both the meson and the baryon correlators at every 10 trajectories at the unitary points where the valence quark masses are equal to the sea quark masses. Light hadron masses are extracted from a single exponential χ^2 fit to the correlators with an exponentially smeared source and a local sink. Figure 6 shows the hadron effective masses at $\kappa_{ud} = 0.13727$ and 0.13781 as

representative cases. We observe clear plateau for the mesons except for the ρ meson and also good signal for the baryons thanks to a large volume. Especially, the Ω baryon has a stable signal, which we use as a physical input to determine the cutoff scale later. The horizontal lines denote the fitting results with an error band of one standard deviation. Their widths represent the fitting ranges. Statistical errors are estimated by the jackknife method. In Fig. 7 we plot binsize dependence of magnitude of error for the mesons and the baryons at $(\kappa_{ud}, \kappa_s) = (0.13727, 0.13640)$. For the pseudoscalar mesons we observe that the magnitude of error gradually increases as the bin size is enlarged up to about 40 MD time, beyond which it stabilizes. For other hadrons we do not find any clear binsize dependence. The data at other hopping parameters show similar behaviors. Based on this observation we choose 50 molecular dynamics time for the jackknife analysis at all the hopping parameters.

We extract the bare quark mass through the axial vector Ward-Takahashi identity (AWI) by

$$am_q^{\text{AWI}} = \lim_{t \rightarrow \infty} \frac{\langle \nabla_4 A_4^{\text{imp}}(t) P(0) \rangle}{2 \langle P(t) P(0) \rangle} \quad (4.1)$$

with P the pseudoscalar density and A_4^{imp} the nonperturbatively $O(a)$ -improved axial vector current[23]. The renormalized quark mass and the pseudoscalar meson decay constant in the continuum $\overline{\text{MS}}$ scheme are defined as follows:

$$m_q^{\overline{\text{MS}}} = \frac{Z_A \left(1 + b_A \frac{m_q^{\text{AWI}}}{u_0} \right)}{Z_P \left(1 + b_P \frac{m_q^{\text{AWI}}}{u_0} \right)} m_q^{\text{AWI}}, \quad (4.2)$$

$$f_{\text{PS}} = 2\kappa u_0 Z_A \left(1 + b_A \frac{m_q^{\text{AWI}}}{u_0} \right) \frac{C_A^s}{C_P^s} \sqrt{\frac{2C_P^l}{m_{\text{PS}}}}. \quad (4.3)$$

Here $C_{A,P}^s$ are the amplitudes extracted from the correlators $\langle A_4^{\text{imp}}(t) P(0) \rangle$ and $\langle P(t) P(0) \rangle$ with an exponentially smeared source and a local sink, while C_P^l is from $\langle P(t) P(0) \rangle$ with a local source and a local sink. The renormalization factors $Z_{A,P}$ and the improvement coefficients $b_{A,P}$ are evaluated perturbatively up to one-loop level[24, 25] with the tadpole improvement.

4.2 Comparison with the previous CP-PACS/JLQCD results

	lattice size	am_π	am_ρ	am_N
PACS-CS	$32^3 \times 64$	0.3220(6)	0.506(2)	0.726(3)
	$[t_{\min}, t_{\max}]$	[13,30]	[10,20]	[10,20]
CP-PACS/JLQCD	$20^3 \times 40$	0.3218(8)	0.516(3)	0.733(4)
	$[t_{\min}, t_{\max}]$	[8,20]	[9,15]	[11,17]

Table 5: PACS-CS and CP-PACS/JLQCD results for π , ρ and nucleon masses at $(\kappa_{ud}, \kappa_s) = (0.13700, 0.13640)$. $[t_{\min}, t_{\max}]$ denotes the fitting range.

We first compare the PACS-CS results on $32^3 \times 64$ with the previous CP-PACS/JLQCD results on $20^3 \times 40$ [1, 2] at $(\kappa_{ud}, \kappa_s) = (0.13700, 0.13640)$. In Fig. 8 we plot the effective masses for the π and the ρ mesons. The PACS-CS and the CP-PACS/JLQCD results are consistent for the π meson,

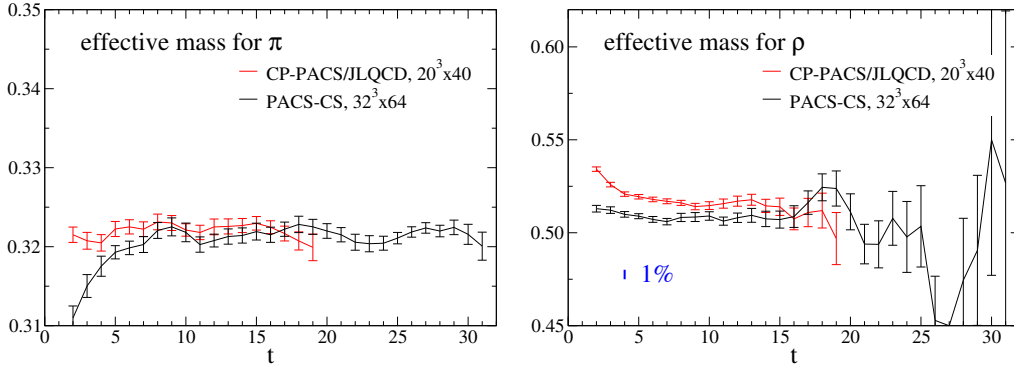


Figure 8: Effective masses for the π (left) and the ρ (right) at $(\kappa_{ud}, \kappa_s) = (0.13700, 0.13640)$. Black and red symbols denote the PACS-CS and the CP-PACS/JLQCD results, respectively.

while a slight deviation is observed for the ρ meson. This is numerically confirmed by the fitting results listed in Table 5, where we employ a single exponential χ^2 fit. The nucleon mass is also given in Table 5. We find 1–2% deviation for the ρ meson and nucleon masses, which could be due to possible finite size effects.

Figure 9 shows the up-down quark mass dependence of $(am_\pi)^2$ and am_ρ with κ_s fixed at 0.13640. For the pion mass we observe that the PACS-CS and the CP-PACS/JLQCD results are smoothly connected as a function of $1/\kappa_{ud}$. On the other hand, the quark mass dependence is not so smooth for the ρ meson. Although this may be attributed to finite size effects, further studies are needed in the ρ channel.

4.3 Chiral analysis on pseudoscalar meson masses and decay constants

We examine the chiral behaviors of the pseudoscalar meson masses and decay constants in comparison with the prediction of chiral perturbation theory (ChPT). Our interest exist in the following points: (i) signals for chiral logarithms, (ii) determination of low energy constants in the chiral lagrangian, (iii) determination of the physical point with the ChPT fit, (iv) estimate of the

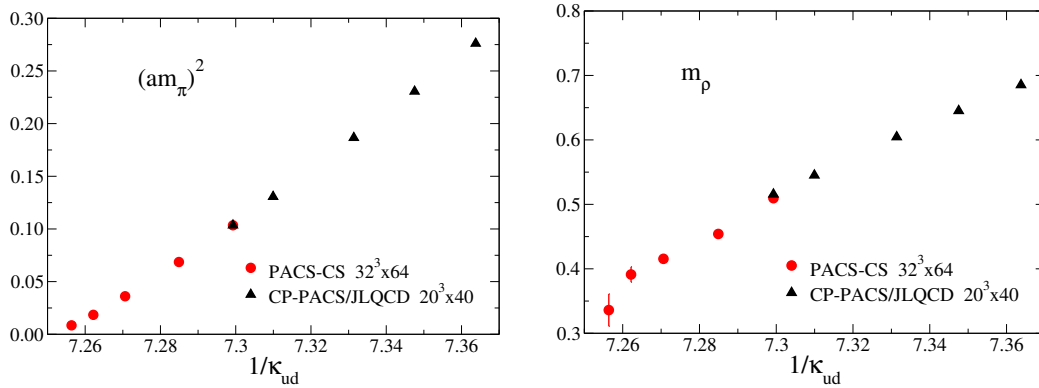


Figure 9: $(am_\pi)^2$ (left) and am_ρ (right) as a function of $1/\kappa_{ud}$. Red and black symbols denote the PACS-CS and the CP-PACS/JLQCD results, respectively.

magnitude of finite size effects based on one-loop calculations of ChPT.

We first recall the one-loop expressions of ChPT for the pseudoscalar meson masses and the decay constants[26]¹:

$$m_\pi^2 = 2\hat{m}B_0 \left\{ 1 + \mu_\pi - \frac{1}{3}\mu_\eta + \frac{B_0}{f_0^2} (16\hat{m}(2L_8 - L_5) + 16(2\hat{m} + m_s)(2L_6 - L_4)) \right\}, \quad (4.4)$$

$$m_K^2 = (\hat{m} + m_s)B_0 \left\{ 1 + \frac{2}{3}\mu_\eta + \frac{B_0}{f_0^2} (8(\hat{m} + m_s)(2L_8 - L_5) + 16(2\hat{m} + m_s)(2L_6 - L_4)) \right\} \quad (4.5)$$

$$f_\pi = f_0 \left\{ 1 - 2\mu_\pi - \mu_K + \frac{B_0}{f_0^2} (8\hat{m}L_5 + 8(2\hat{m} + m_s)L_4) \right\}, \quad (4.6)$$

$$f_K = f_0 \left\{ 1 - \frac{3}{4}\mu_\pi - \frac{3}{2}\mu_K - \frac{3}{4}\mu_\eta + \frac{B_0}{f_0^2} (4(\hat{m} + m_s)L_5 + 8(2\hat{m} + m_s)L_4) \right\}, \quad (4.7)$$

where $\hat{m} = (m_u + m_s)/2$ and $L_{4,5,6,8}$ are the low energy constants, and μ_{PS} is the chiral logarithm defined by

$$\mu_{\text{PS}} = \frac{1}{32\pi^2} \frac{m_{\text{PS}}^2}{f_0^2} \ln \left(\frac{m_{\text{PS}}^2}{\mu^2} \right) \quad (4.8)$$

with μ the renormalization scale. There are six unknown low energy constants $B_0, f_0, L_{4,5,6,8}$ in the expressions above. The low energy constants are scale-dependent so as to cancel that of the chiral logarithm (4.8). We determine these parameters by making a simultaneous fit for m_π^2, m_K^2, f_π and f_K .

We also consider the contributions of the finite size effects based on ChPT. At the one-loop level the finite size effects defined by $R_X = (X(L) - X(\infty))/X(\infty)$ for $X = m_\pi, m_K, f_\pi, f_K$ are given by [27]:

$$R_{m_\pi} = \frac{1}{4}\xi_\pi \tilde{g}_1(\lambda_\pi) - \frac{1}{12}\xi_\eta \tilde{g}_1(\lambda_\eta), \quad (4.9)$$

$$R_{m_K} = \frac{1}{6}\xi_\eta \tilde{g}_1(\lambda_\eta), \quad (4.10)$$

$$R_{f_\pi} = -\xi_\pi \tilde{g}_1(\lambda_\pi) - \frac{1}{2}\xi_K \tilde{g}_1(\lambda_K), \quad (4.11)$$

$$R_{f_K} = -\frac{3}{8}\xi_\pi \tilde{g}_1(\lambda_\pi) - \frac{3}{4}\xi_K \tilde{g}_1(\lambda_K) - \frac{3}{8}\xi_\eta \tilde{g}_1(\lambda_\eta) \quad (4.12)$$

with

$$\xi_{\text{PS}} \equiv \frac{m_{\text{PS}}^2}{(4\pi f_\pi)^2}, \quad \lambda_{\text{PS}} \equiv m_{\text{PS}}L, \quad \tilde{g}_1(x) = \sum_{n=1}^{\infty} \frac{4m(n)}{\sqrt{nx}} K_1(\sqrt{nx}), \quad (4.13)$$

where K_1 is the Bessel function of the second kind and $m(n)$ denotes the multiplicities in the expression of $n = n_x^2 + n_y^2 + n_z^2$. With the use of these formulae we estimate the possible finite size effects in our results.

Before presenting our fitting results, it is instructive to compare the PACS-CS and the CP-PACS/JLQCD results for $(am_\pi)^2/(am_{\text{ud}}^{\text{AWI}})$ and f_K/f_π . In Fig. 10 we plot them as a function of

¹ f_π is normalized as 92.4 MeV in these expressions, while our results are presented in the $f_\pi = 130.7$ MeV normalization.

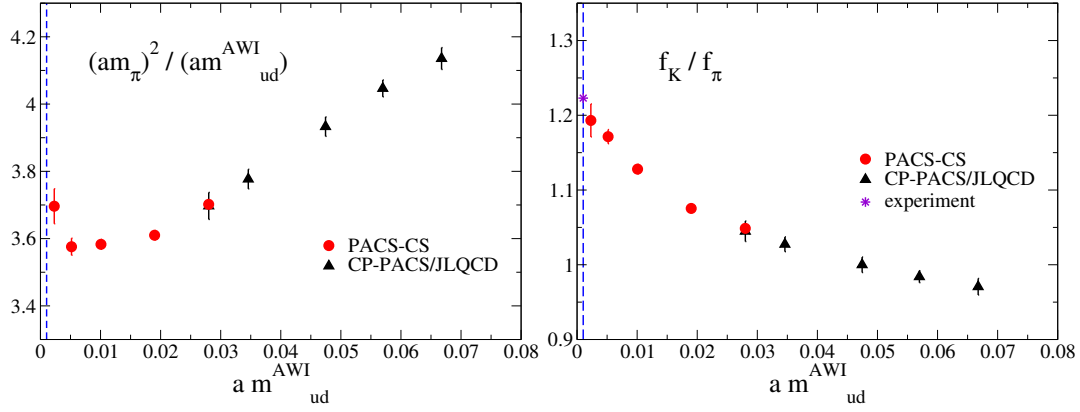


Figure 10: Comparison of the PACS-CS (red) and the CP-PACS/JLQCD (black) results for $(am_\pi)^2 / (am_{ud}^{AWI})$ (left) and f_K / f_π (right) as a function of am_{ud}^{AWI} . κ_s is fixed at 0.13640. Vertical lines denote the physical point and star symbol represents the experimental value.

am_{ud}^{AWI} with κ_s fixed at 0.13640. The PACS-CS and the CP-PACS/JLQCD results are denoted by the red and the black symbols, respectively. The two sets of data together show a smooth behavior as a function of am_{ud}^{AWI} , and at $\kappa_{ud} = 0.13700$ ($am_{ud}^{AWI} = 0.028$) they show good consistency. It is important to observe that an almost linear quark mass dependence of the CP-PACS/JLQCD results for heavier up-down quark masses changes into a convex behavior, both for $(am_\pi)^2 / (am_{ud}^{AWI})$ and f_K / f_π , as the quark mass is lowered in the PACS-CS runs. This is a characteristic feature expected from the ChPT prediction in the small quark mass region due to the chiral logarithm. This curvature drives up the ratio f_K / f_π toward the experimental value as the physical point is approached.

Let us apply the ChPT formulae (4.4)–(4.7) to our results at four points $(\kappa_{ud}, \kappa_s) = (0.13781, 0.13640)$, $(0.13770, 0.13640)$, $(0.13754, 0.13640)$, $(0.13754, 0.13660)$. For these points, the ρ meson mass satisfies the condition that $m_\rho > 2m_\pi$. The measured bare AWI quark masses are used for \hat{m} and m_s in eqs.(4.4)–(4.7). The heaviest pion mass at $(\kappa_{ud}, \kappa_s) = (0.13754, 0.13640)$ is about 430 MeV with the use of the cutoff determined below. We summarize the pion masses and the unrenormalized AWI quark masses in Table 6. The fit results are shown in Fig. 11, where the black solid lines are drawn with κ_s fixed at 0.13640 and the black dotted lines are for $\kappa_s = 0.13660$. The red solid symbols represent the extrapolated values at the physical point whose determination is explained in

κ_{ud}	κ_s	am_π	am_{ud}^{AWI}	am_s^{AWI}
0.13700	0.13640	0.32196(62)	0.02800(20)	0.04295(30)
0.13727	0.13640	0.26190(66)	0.01895(13)	0.04061(18)
0.13754	0.13640	0.18998(56)	0.01020(11)	0.03876(18)
	0.13660	0.17934(78)	0.00908(7)	0.03257(17)
0.13770	0.13640	0.13591(88)	0.00521(9)	0.03767(10)
0.13781	0.13640	0.08989(291)	0.00227(16)	0.03716(20)

Table 6: Pion masses and unrenormalized AWI quark masses.

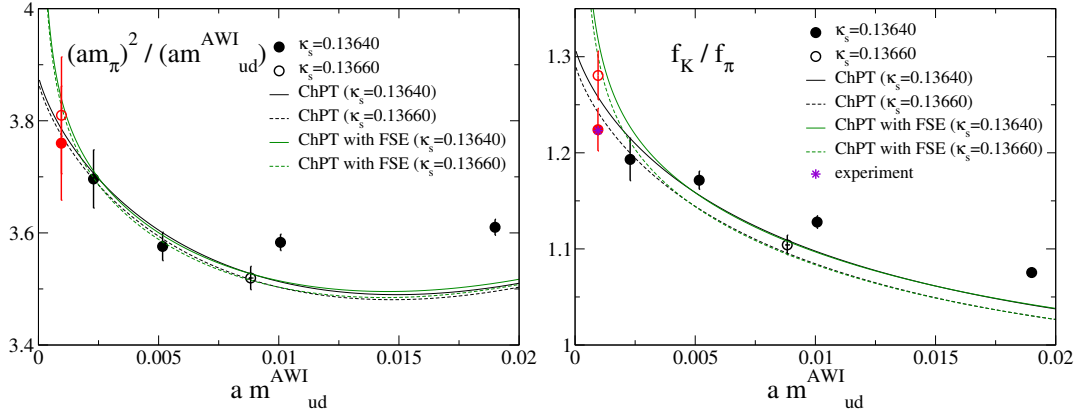


Figure 11: Fitting results for $(am_\pi)^2 / (am_{ud}^{\text{AWI}})$ (left) and f_K / f_π (right). Red solid (open) symbols denote the extrapolated values at the physical point by the ChPT formulae without (with) the finite size effects.

Sec. 4.4 below. The heaviest point at $(\kappa_{ud}, \kappa_s) = (0.13754, 0.13640)$ is not well described by ChPT both for $(am_\pi)^2 / (am_{ud}^{\text{AWI}})$ and f_K / f_π , and $\chi^2/\text{d.o.f.}$ is rather large (see Table 7).

$L_i(\mu = m_\eta)$	PACS-CS	PACS-CS with FSE	exp. value[28]	MILC[29]
L_4	0.25(11)	0.23(12)	0.27 ± 0.8	0.1(2)(2)
L_5	2.28(13)	2.29(14)	2.28 ± 0.1	2.0(3)(2)
$2L_6 - L_4$	0.16(4)	0.16(4)	0 ± 1.0	0.5(1)(2)
$2L_8 - L_5$	-0.59(5)	-0.60(5)	0.18 ± 0.5	-0.1(1)(1)
$\chi^2/\text{d.o.f.}$	2.1(1.4)	2.1(1.4)		

Table 7: Results for the low energy constants together with the phenomenological estimates[28] and the MILC results[29].

The results for the low energy constants are presented in Table 7 where the phenomenological values with the experimental inputs[28] and the MILC results[29] are also given for comparison. The renormalization scale is chosen to be $m_\eta = 0.547$ GeV. For L_4 and L_5 governing the behavior of f_π, f_K , our results show good agreement with both the phenomenological estimates and the MILC results. On the other hand, some discrepancies are observed between three results for $2L_6 - L_4$ and $2L_8 - L_5$ which enter into the ChPT formulae for m_π^2 and m_K^2 .

In Fig. 11 we also draw the ChPT fit results including the finite size effects. The green solid lines are drawn for $\kappa_s = 0.13640$ and the green dotted ones for $\kappa_s = 0.13660$. The fit curves with and without the finite size effects are almost degenerate for $am_{ud}^{\text{AWI}} > 0.003$, but deviations appear closer to the physical point, for which the extrapolated values are plotted by the open and solid red symbols. This feature is understood by Fig. 12 where we plot the magnitude of R_X for $X = m_\pi, m_K, f_\pi, f_K$ with $L = 2.8$ fm as a function of m_π (we note that $R_{m_{PS}} > 0$ and $R_{f_{PS}} < 0$). The finite size effects are less than 2% for m_{PS} and f_{PS} at our simulation points. For m_{PS} this is true even at the physical point, while for f_π the finite size effects cause the value to decrease by 4%.

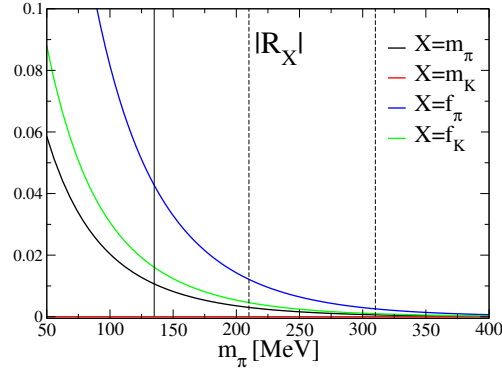


Figure 12: $|R_X|$ ($R_{m_{PS}} > 0$ and $R_{f_{PS}} < 0$) for $X = m_\pi, m_K, f_\pi, f_K$ with $L = 2.8$ fm as a function of m_π . Solid vertical line denotes the physical point and the dotted ones are for our simulation points.

4.4 Physical point and light hadron spectrum

In order to determine the up-down and the strange quark masses and the lattice cutoff we need three physical inputs. We try the following two cases: m_π, m_K, m_Ω and m_π, m_K, m_ϕ . The choice of m_Ω has theoretical and practical advantages: the Ω baryon is stable in the strong interactions and its mass, being composed of three strange quarks, is determined with good precision with small finite size effects. We also choose m_ϕ for comparison. We employ the NLO ChPT formulae for the chiral extrapolations of m_π, m_K, f_π and f_K . A simple linear formula $m_{\text{had}} = c_0 + c_1 \cdot m_{\text{ud}}^{\text{AWI}} + c_2 \cdot m_s^{\text{AWI}}$ is used for the other hadron masses, employing data in the same range $\kappa_{\text{ud}} \geq 0.13754$ as for the pseudoscalar mesons. In Fig. 13 we show the linear chiral extrapolations for m_ϕ and m_Ω . The solid lines are drawn with κ_s fixed at 0.13640 and the dotted ones are for $\kappa_s = 0.13660$. We observe that the quark mass dependences for m_ϕ and m_Ω at $\kappa_{\text{ud}} \geq 0.13754$ are well described by the linear function.

The results for the quark masses and the lattice cutoff are listed in Table 8, where the errors are statistical. The two sets of results are consistent within the error. The quark masses are smaller than the recent estimates in the literature. We note, however, that we employed the perturbative renor-

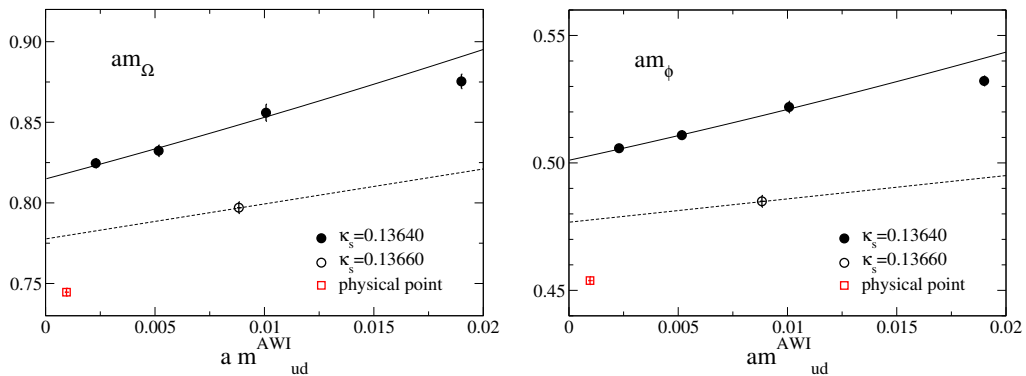


Figure 13: Linear chiral extrapolation for am_Ω (left) and am_ϕ (right). Solid (dotted) lines are drawn with $\kappa_s = 0.13640$ (0.13660). Red open symbols denote the extrapolated values at the physical point with a linear form.

input	a^{-1} [GeV]	m_{ud}^{MS} [MeV]	m_s^{MS} [MeV]	f_π	f_K	f_K/f_π
m_Ω	2.256(81)	2.37(11)	69.1(25)	144(6)	175(6)	1.219(22)
m_ϕ	2.248(76)	2.38(11)	69.4(25)	143(6)	175(5)	1.219(21)

Table 8: Cutoff, renormalized quark masses, pseudoscalar meson decay constants determined with m_Ω and m_ϕ inputs.

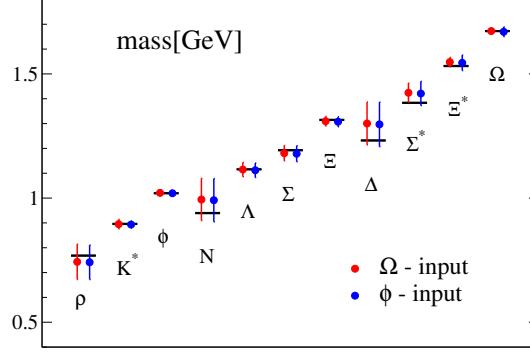


Figure 14: Light hadron spectrum extrapolated at the physical point with Ω -input (red) and ϕ -input (blue). Horizontal bars denote the experimental values.

malization factors to one-loop level which may contain a sizable uncertainty. A nonperturbative calculation of the renormalization factor is in progress using the Schrödinger functional scheme.

In Table 8 we also present predictions for the pseudoscalar meson decay constants at the physical point using the physical quark masses and the cutoff determined above, which should be compared with the experimental values $f_\pi = 130.7$ MeV, $f_K = 159.8$ MeV, $f_K/f_\pi = 1.223$. A 10% discrepancy in the magnitude of f_π and f_K might be due to use of one-loop perturbative Z_A since the ratio shows a good agreement. A nonperturbative calculation of Z_A is also in progress.

In Fig. 14 we compare the light hadron spectrum extrapolated to the physical point with the experiment. The results for the Ω -input and the ϕ -input are consistent with each other, and both are in agreement with the experiment albeit errors are still not small for some of the hadrons. This is an encouraging result. However, further work is needed since cutoff errors of $O((a\Lambda_{\text{QCD}})^2)$ are present in our results.

5. ρ - $\pi\pi$ mixing

Since our simulations are carried out at sufficiently small up-down quark masses, it would be interesting to investigate the ρ - $\pi\pi$ mixing effects. We find that the rest mass m_ρ is always smaller than the two-pion energy $2\sqrt{m_\pi^2 + (2\pi/L)^2}$ for all the hopping parameters, and hence the ρ meson at rest cannot decay into two pions. However, as illustrated in Fig. 15, for a moving ρ with a unit of momentum, *i.e.*, its energy $\sqrt{m_\rho^2 + (2\pi/L)^2}$ becomes larger than the energy of a moving pion and a pion at rest given by $\sqrt{m_\pi^2 + (2\pi/L)^2} + m_\pi$ when the up-down quark mass is sufficiently reduced.

Let us consider two types of the ρ meson propagator with the momentum $2\pi/L$: $\rho_\parallel(2\pi/L)$ with polarization parallel to the spatial momentum and $\rho_\perp(2\pi/L)$ with polarization perpendicular

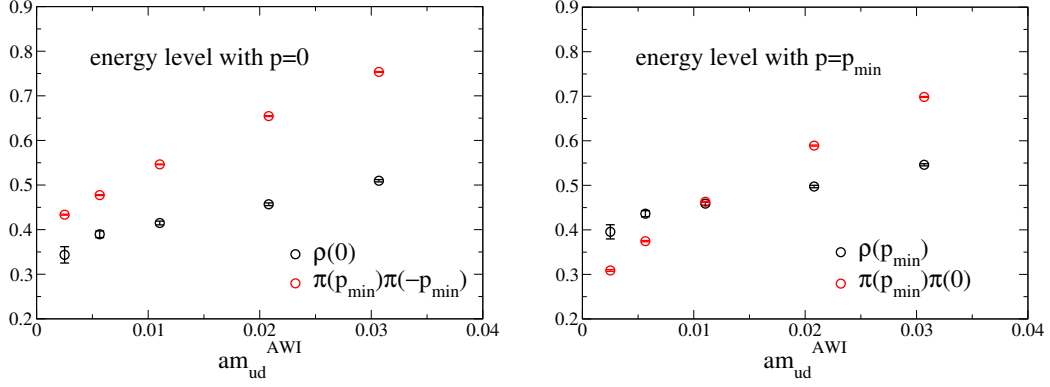


Figure 15: Energy levels of the ρ meson and the two pion states without the total momentum $p = 0$ (left) and with $p = p_{\min} \equiv 2\pi/L$ (right) as a function of the up-down quark mass. κ_s is fixed at 0.13640.

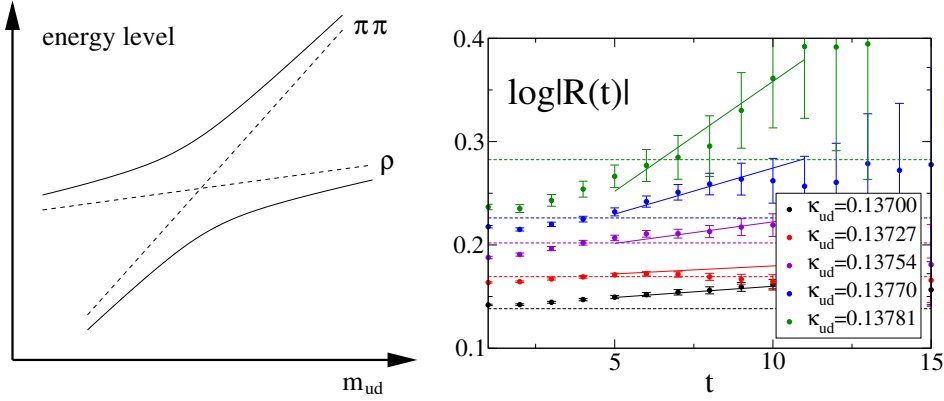


Figure 16: Schematic view of ρ and $\pi\pi$ energy levels due to mixing effects (left) and time dependence of the R function (right).

to the spatial momentum. Phenomenologically the ρ - $\pi\pi$ coupling is described by $g_{\rho\pi\pi}\varepsilon_{abc}\rho_{\mu}^a\pi^b\partial_{\mu}\pi^c$, which favors $\rho_{\parallel}(2\pi/L) \rightarrow \pi(2\pi/L)\pi(0)$ to $\rho_{\perp}(2\pi/L) \rightarrow \pi(2\pi/L)\pi(0)$. We expect that the $\rho_{\parallel}(2\pi/L)$ propagator is more strongly affected by the mixing effects than the $\rho_{\perp}(2\pi/L)$ correlator. Since the mixing effects push up the upper energy level further and push down the lower energy level as shown in Fig. 16, they could be detected by measuring the R function defined by

$$R(t) = \frac{\langle \rho_{\parallel}(\vec{p}, t) \rho_{\parallel}^{\dagger}(\vec{p}, 0) \rangle}{\langle \rho_{\perp}(\vec{p}, t) \rho_{\perp}^{\dagger}(\vec{p}, 0) \rangle} \xrightarrow{\text{large } t} Z e^{-(E_{\rho_{\parallel}} - E_{\rho_{\perp}})t}. \quad (5.1)$$

In Fig. 16 we plot $\log|R(t)|$ as a function of t . The dotted horizontal lines denote $R(t) = (E/m_{\rho})^2$, which is determined kinematically in the mixing-free case. The solid lines represent the fitting results with a single exponential form over $5 \leq t \leq 11$. The data show clear positive slopes which indicate $E_{\rho_{\parallel}} < E_{\rho_{\perp}}$. We also observe that the magnitude of the energy difference is rather small for $\kappa_{ud} \leq 0.13754$, while it grows rapidly as the up-down quark mass is reduced for $\kappa_{ud} > 0.13754$. This feature may suggest that the $\langle \rho_{\parallel}(\vec{p}, t) \rho_{\parallel}^{\dagger}(\vec{p}, 0) \rangle$ correlator is getting dominated by the $\pi\pi$ state toward the smaller up-down quark masses. In order to obtain a definite conclusion, we need more

detailed investigations with increased statistics.

6. Summary

We have presented a status report of the PACS-CS project which aims at a 2+1 flavor lattice QCD simulation toward the physical point. With the aid of the DDHMC algorithm for the up-down quarks we have reached $m_\pi = 210$ MeV, which roughly corresponds to $m_{\text{ud}}^{\overline{\text{MS}}}(\mu = 2 \text{ GeV}) = 5.6$ MeV, on a $32^3 \times 64$ lattice using the $O(a)$ -improved Wilson quarks. Thanks to the enlarged volume compared to the previous CP-PACS/JLQCD work, we obtain good signals not only for the meson masses but also for the baryon masses. Our results for the hadron spectrum at the physical point show a good agreement with the experimental values.

At present we have just started the simulation at the physical point. We are also calculating the nonperturbative renormalization factors for the quark masses and the pseudoscalar meson decay constants in order to remove perturbative uncertainties in these important quantities. Once these calculations are accomplished, the next step is to investigate the finite size effects at the physical point, and then to reduce the discretization errors by carrying out calculations at finer lattice spacings.

Acknowledgment

We would like to thank all the collaboration members for discussions and, in particular, A. Ukawa for a careful reading of this report. Numerical calculations for the present work have been carried out under the “Interdisciplinary Computational Science Program” in Center for Computational Sciences, University of Tsukuba. This work is supported in part by Grants-in-Aid for Scientific Research from the Ministry of Education, Culture, Sports, Science and Technology (Nos. 13135204, 15540251, 17340066, 17540259, 18104005, 18540250, 18740139).

References

- [1] CP-PACS and JLQCD Collaborations, T. Ishikawa *et al.*, PoS (LAT2006) 181.
- [2] CP-PACS and JLQCD Collaborations, T. Ishikawa *et al.*, hep-lat/0704.193.
- [3] CP-PACS and JLQCD Collaborations, S. Aoki *et al.*, Phys. Rev. **D73** (2006) 034501.
- [4] Y. Iwasaki, preprint, UTHEP-118 (Dec. 1983), unpublished.
- [5] JLQCD Collaborations, S. Aoki *et al.*, Phys. Rev. **D65** (2002) 094507.
- [6] PACS-CS Collaboration, S. Aoki *et al.*, PoS (LAT2005) 111.
- [7] PACS-CS Collaboration, A. Ukawa *et al.*, PoS (LAT2006) 039.
- [8] PACS-CS Collaboration, Y. Kuramashi *et al.* PoS (LAT2006) 029.
- [9] M. Lüscher, JHEP **0305** 052 (2003); Comput. Phys. Commun. **165** (2005) 199.
- [10] A. Kennedy, Nucl. Phys. **B** (Proc. Suppl.) **140** (2005) 190.
- [11] PACS-CS Collaboration, K-I. Ishikawa *et al.* PoS (LAT2006) 027.
- [12] PACS-CS Collaboration, N. Ukita *et al.*, PoS (LAT2007) 138.

- [13] PACS-CS Collaboration, D. Kadoh *et al.*, PoS (LAT2007) 109.
- [14] L. Del Debbio *et al.*, JHEP **0602** (2006) 011.
- [15] L. Del Debbio *et al.*, JHEP **0702** 056 (2007); JHEP **0702** (2007) 082.
- [16] J. C. Sexton and D. H. Weingarten, Nucl. Phys. **B380** (1992) 665.
- [17] M. Lüscher, Comput. Phys. Commun. **156** (2004) 209.
- [18] A. Ukawa, Nucl. Phys. **B** (Proc. Suppl.) **106** (2002) 195.
- [19] CP-PACS Collaboration, A. Ali Khan *et al.*, Phys. Rev. **D65** (2002) 054505.
- [20] M. Hasenbusch, Phys. Lett. **B519** (2001) 177.
- [21] M. Hasenbusch and K. Jansen, Nucl. Phys. **B659** (2003) 299.
- [22] ALPHA Collaboration, K. Jansen and R. Sommer, Nucl. Phys. **B530** (1998) 185.
- [23] CP-PACS/JLQCD and ALPHA Collaborations, T. Kaneko *et al.*, JHEP **0704** (2007) 092.
- [24] S. Aoki *et al.*, Phys. Rev. **D58** (1998) 074505.
- [25] Y. Taniguchi and A. Ukawa, Phys. Rev. **D58** (1998) 114503.
- [26] J. Gasser and H. Leutwyler, Ann of Phys. **158** (1984) 142; Nucl. Phys. **B250** (1985) 465.
- [27] G. Colangelo, S. Dürr and C. Haefeli, Nucl. Phys. **B721** (2005) 136.
- [28] G. Amorós, J. Bijnens and P. Talavera, Nucl. Phys. **B602** (2001) 87.
- [29] C. Bernard *et al.*, arXiv:hep-lat/0611024.